Geophysical Journal International

Geophys. J. Int. (2026) **244,** 1–20
Advance Access publication 2026 January 10
Research Paper

https://doi.org/10.1093/gji/ggag006

High-Resolution Spatiotemporal Monitoring of Secondary Microseisms via Multi-Array Analysis

Yajian Gao [1], Andreas Rietbrock [1], Frederik Tilmann [2,3] and Edmond Dushi [4]

[1] *Geophysical Institute, Karlsruhe Institute of Technology, Karlsruhe, 76187, Germany. E-mail: ya-jian.gao@kit.edu*
[2] *GFZ Helmholtz Centre for Geosciences, Potsdam, 14473, Germany*
[3] *Institute for Geological Sciences, Freie Universität Berlin, Berlin, 12249, Germany*
[4] *Institute of Geosciences, Polytechnic University of Tirana, Tirana, 1024, Albania*

Accepted 2025 December 29. Received 2025 December 19; in original form 2025 May 30

SUMMARY

This study presents a workflow to monitor spatiotemporal variations of the secondary microseisms using multi-array analysis. We employ ambient-noise cross-correlation beamforming (CC beamforming) across three dense seismic networks with different instrument responses: ANTICS in Albania (nodal-geophone and broadband), Hi-net in Japan (short-period) and SCSN (broadband) in Southern California. Independent of their instrumentation, these networks enable us to track the spatial and temporal evolution of secondary microseism sources in the Northern Hemisphere from autumn 2022 to spring 2023. The workflow involves continuous data pre-processing for different instrumented sensors, ambient-noise cross-correlation, beamforming and beam-power back-projection into a global map. We also propose sliding-window raw-data beamforming (RA beamforming) for the continuous broad-band data in this workflow to record the absolute amplitudes of secondary microseisms recorded by ANTICS. Joint CC beamforming analysis across the three different networks improves the resolution of ambient-noise source localization and displays high consistency with the equivalent vertical force at the ocean floor. The results indicate that secondary microseism sources in the Northern Hemisphere are predominantly driven by winter storms in the northern Atlantic and northern Pacific. The relative and absolute amplitudes of the beam-power for the northern Atlantic are also extracted from CC beamforming based on geophone sensors and RA beamforming based on broad-band instruments from ANTICS, respectively. Both approaches provide robust estimates of microseism strength in the northern Atlantic, with CC beamforming displaying a higher correlation with the modelled ocean floor equivalent forces. This study confirms the feasibility of using cost-effective nodal seismic arrays for detailed monitoring of secondary microseisms and highlights the potential for integrating multi-array seismic data with oceanographic models for an improved understanding of seismic noise generation and propagation.

Key words: Secondary microseism; Ambient Noise Beamforming.

1 INTRODUCTION

Seismic ambient noise has been studied thoroughly over the last few decades, and significant success has been achieved involving the extraction of empirical Green's functions for seismic tomography, most often surface wave tomography involving mapping the thickness and properties of sedimentary layers, the crust and even the upper mantle (e.g. N.M. Shapiro *et al.* 2005; W. Shen *et al.* 2013). Less common are studies which extract seismic body waves from ambient noise cross-correlation, for example, to map the mantle discontinuities (e.g. P. Poli *et al.* 2012; H.A. Pedersen *et al.* 2022; Y. Lu *et al.* 2023) and global propagation and imaging (e.g. P. Boué *et al.* 2013, 2014; P. Boué & L. Tomasetto 2023).

Even earlier, the heterogeneous distribution and physical nature of ambient noise sources were studied (e.g. M.S. Longuet-Higgins 1950; S. Chevrot *et al.* 2007; S. Kedar *et al.* 2008; F. Ardhuin *et al.* 2011; Q. Liu *et al.* 2016). Natural seismic noise is dominated by sources generated in the oceans (e.g. F. Ardhuin *et al.* 2015; T. Tanimoto & A. Anderson 2023). Its amplitude is highest in the microseism band (3–30 s), which is generally subdivided into primary and secondary microseisms according to their dominant periods.

The primary microseism dominates in the period band from 10 to 30 s, whereas the secondary microseism contributes mainly to

the noise between 3 and 10 s (J. Peterson 1993; F. Ardhuin *et al.* 2015; T. Tanimoto & A. Anderson 2023). Primary microseisms are generated where pressure fluctuations from ocean waves interact with variations in seafloor bathymetry, typically in shallow-water regions (e.g. P.D. Bromirski *et al.* 2017; D.E. McNamara & R.I. Boaz 2019). They occur at the same frequency as the generating ocean waves (single-frequency microseisms) and thus carry information about near-shore and coastal wave dynamics. In contrast, secondary microseisms have twice the frequency of incoming ocean waves (M.S. Longuet-Higgins 1950) due to the nonlinear interaction of two opposing ocean wave trains with similar dominant periods (e.g. M.S. Longuet-Higgins 1950; K. Hasselmann 1963; N. Nakata *et al.* 2019). The secondary microseisms also usually display the most energetic amplitude in the seismic ambient noise spectrum (e.g. J. Peterson 1993; N. Nakata *et al.* 2019; Q. Liu *et al.* 2024). Though the depth range of ocean waves is confined to the upper 100–200 m, the pressure associated with the standing wave caused by wave–wave interaction can exert pressure at any depth below where two interacting wave trains meet at the sea surface. Therefore, this process can generate seismic waves at the ocean floor (L. Gualtieri *et al.* 2014, 2015; T. Tanimoto & A. Anderson 2023; L. Tomasetto *et al.* 2025).

Secondary microseisms can be caused by three types of physical wave configurations (M.J. Obrebski *et al.* 2012; D.E. McNamara & R.I. Boaz 2019). The strongest type of secondary microseism source comes from the interaction of two ocean wave systems that have the same dominant frequency but opposite directions (e.g. F. Ardhuin *et al.* 2011; D.E. McNamara & R.I. Boaz 2019; L. Li *et al.* 2020). This type often occurs in the open ocean when one ocean swell meets the opposite ocean waves from another swell, which could be previously generated by the same storm or uncorrelated storms (e.g. M.J. Obrebski *et al.* 2012). The two other sources are related to oblique ocean waves that meet the main wave direction as well as the interaction of the incoming ocean waves with the reflected waves from the coastline (F. Ardhuin *et al.* 2011; F. Ardhuin & A. Roland 2012). All three mechanisms can create a pressure wave that propagates down to the ocean floor. The direct *P* (pressure wave) in the water layer, the reflected *P* at the ocean floor and the refracted *P* (along the ocean floor and then returning into the water layer), all could be further amplified by multiple reflections at the sea surface (L. Gualtieri *et al.* 2015; N. Nakata *et al.* 2019). Even though a large part of the energy remains within the water layer, a part of the energy can be transmitted across the sea floor into the solid earth as body waves, that is, the transmitted *P* and *P*-to-*S* converted wave. The sum of multiple reflected *P* waves in the water layer can generate frequency-dependent resonance effects in the source region, which are called 'source site effect' (L. Gualtieri *et al.* 2013, 2014, 2015). In addition to body waves, Rayleigh and Love waves can be generated beneath the ocean floor through coupling, conversion and resonance effects. In this study, we focus on the body wave, especially the *P* wave. For a more detailed derivation of the excitation of the surface wave from secondary microseism, readers are referred to M.S. Longuet-Higgins (1950); F. Ardhuin *et al.* (2011); E. Stutzmann *et al.* (2012); L. Tomasetto *et al.* (2025) for Rayleigh waves, and L. Gualtieri *et al.* (2020); H. Xiao *et al.* (2021) for Love waves. The efficiency of this conversion from ocean acoustic waves to elastic waves beneath the ocean floor is thus influenced by the water depth, the slope of the sea floor and the sediment thickness (L. Gualtieri *et al.* 2013, 2014, 2015; N. Nakata *et al.* 2019; Q. Liu *et al.* 2020).

Thanks to significant efforts in developing the oceanographic hindcast model WAVEWATCHIII (WW3) by IFREMER (H. Tolman *et al.* 2014), it is possible to roughly compare the significant wave height and spectral density of the wave-induced pressure just below the sea surface (hereafter, surface spectral density) with the location of ambient noise sources from seismological observations (e.g. K. Nishida & R. Takagi 2016; V. Farra *et al.* 2016; L. Li *et al.* 2020; H. Xiao *et al.* 2021; J. Igel *et al.* 2021). However, significant wave height or ocean spectral density (WW3 hindcast model) should not be used directly as a proxy for the ambient noise source because coupling and resonance are not taken into account. The recent systematic ambient noise reconstruction package Wave Model Sources of Ambient Noise (WMSAN) (L. Tomasetto *et al.* 2025) reformulates and summarizes the synthetic ambient noise physics based on WW3 products. WMSAN additionally considers bathymetry and wave-induced pressure in the water column. WMSAN could help seismologists reconstruct synthetic secondary microseism source maps, synthetic spectrograms and synthetic cross-correlations with considerations of different seismic wave types (e.g. *P*, *SV* and Rayleigh waves). Therefore, in this study, we explore the application of these recent developments to the calculation of the synthetic secondary microseism generation (equivalent force) on the ocean floor and compare it with the secondary microseism observations from multiple data sets.

However, secondary microseism source information is typically embedded within continuous seismic recordings together with regional and teleseismic earthquakes and anthropogenic noise (T. Lecocq *et al.* 2020). Extracting the location and strength of secondary microseism sources is therefore a central challenge for spatiotemporal microseism analysis. Several approaches have been proposed to address this problem. These include temporal amplitude analysis of seismic records (F. Ardhuin *et al.* 2011), beamforming-based methods (e.g. K.D. Koper *et al.* 2009; G.G. Euler *et al.* 2014; M. Gal *et al.* 2015; K. Nishida & R. Takagi 2022), elliptical polarization analysis (e.g. K.D. Koper & V.L. Hawley 2010; Y. Lu *et al.* 2021), and adjoint full-waveform inversion (FWI) applied to ambient-noise cross-correlations, primarily for Rayleigh waves (K. Sager *et al.* 2018; J. Igel *et al.* 2021). In most cases, the inferred microseism source characteristics are subsequently compared with oceanographic proxies such as significant wave height or surface pressure spectral density derived from the WAVEWATCH III (WWIII) model. Among these approaches, raw-data beamforming (RA beamforming) and back-projection are widely used for detecting ambient-noise sources but typically require explicit exclusion of earthquake-contaminated time windows and spectral whitening to suppress transient seismic signals and local cultural noise (e.g. M. Gal *et al.* 2015; H. Xiao *et al.* 2021; K. Nishida & R. Takagi 2022). In contrast, cross-correlation beamforming (CC beamforming) offers an alternative strategy that inherently suppresses incoherent transient signals through cross-correlation and enables flexible time-windowing and station-pair selection (G.G. Euler *et al.* 2014). The diagonal elements of the cross-spectral density matrix correspond to autocorrelation spectra and can be excluded, preventing bias from incoherent noise that would otherwise contaminate the beamforming results. For a detailed comparison between conventional RA beamforming and CC beamforming, the reader is referred to G.G. Euler *et al.* (2014) and E. Ruigrok *et al.* (2017).

In this study, we try to extract robust ambient noise cross-correlations for three different instrumented networks, including broad-band, short-period (K. Nishida & R. Takagi 2016), and geophone-type (F. Cheng *et al.* 2021) seismometer recordings, and

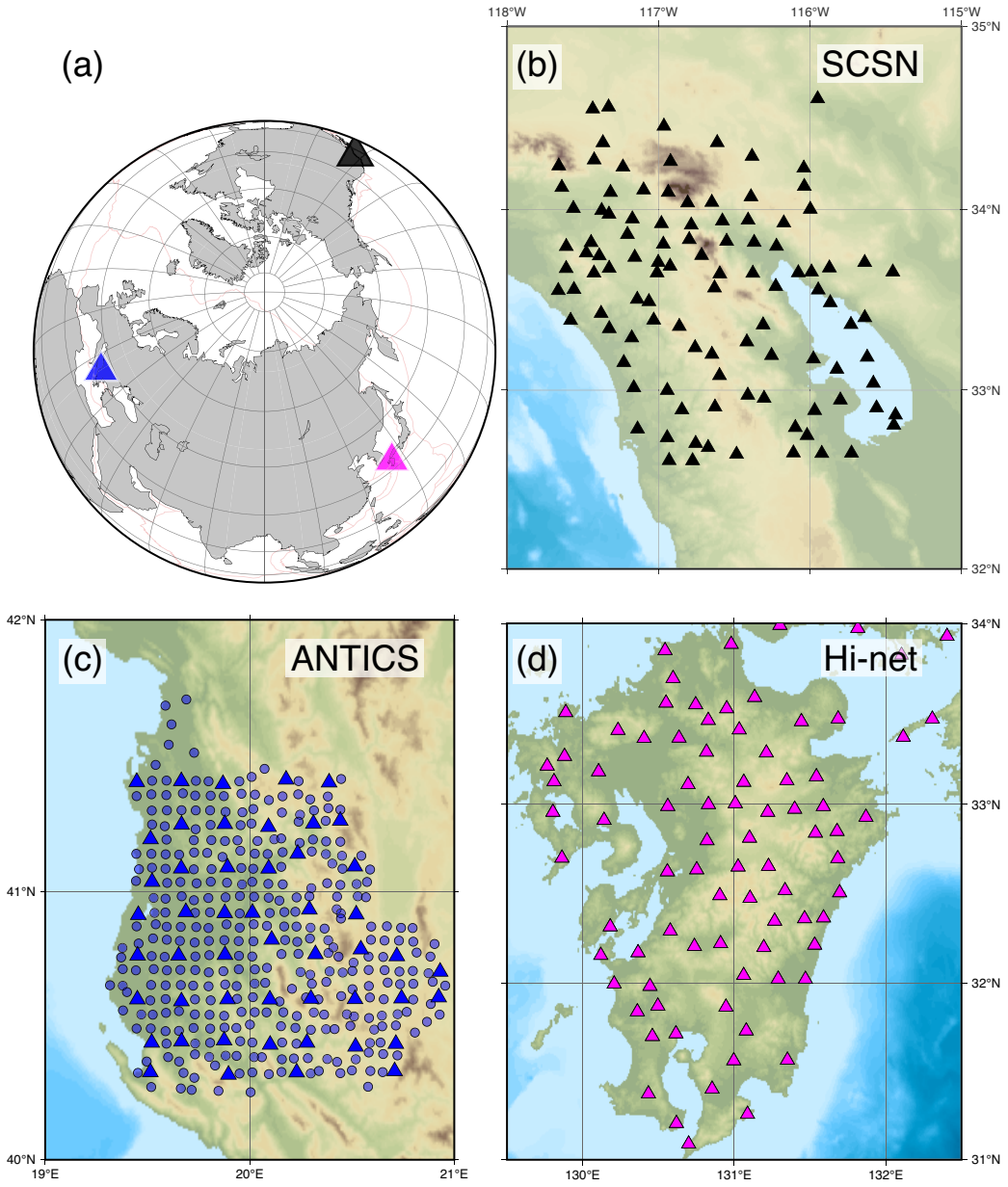

Figure 1. Map for three dense seismic networks: (a): Global view for three networks; (b) Southern California Seismic Network (SCSN, network code CI) (c) ANTICS (Blue triangles denote broad-band seismometers, whereas blue circles represent nodal-array geophones, network code X3) (d) Hi-net short-period instruments (network code N).

apply CC beamforming to track the evolution of secondary microseisms. For all recording types, we are able to generate 3-hr and daily secondary microseism maps. We further perform multi-array CC beamforming, which combines the individual maps. The results are further compared with the secondary microseism from SANS model (J. Igel *et al.* 2021), significant wave heights, surface spectral densities from WW3 and the ocean-floor equivalent forces calculated using WMSAN (L. Tomasetto *et al.* 2025), which directly predicts the strength of microseisms generated, accounting for source site effects. Our multi-array CC beamforming can better constrain the spatiotemporal evolution of the secondary microseism (5–10 s) in the Northern Hemisphere with 3-hr resolution and correlates well with the computed secondary microseism generation on the ocean floor (WMSAN). To further analyse the temporal changes in the strength of the secondary microseism in the northern Atlantic, we extract the relative and absolute beam-power amplitudes from the ANTICS data as a function of time over 9 months. CC beamforming performs better than RA beamforming in constraining the winter secondary microseism in the northern Atlantic when the Mediterranean Sea is also experiencing enhanced storm activity affecting the regional noise field.

2 DATA

In this study (Fig. 1), we analyse continuous seismic waveform data from the permanent short-period Hi-net array (Y. Okada *et al.* 2004; K. Obara *et al.* 2005) in Kyushu, Japan, the broad-band stations from Southern California Seismic Network (SCSN, California Institute of Technology (Caltech), 1926), and the recent dense nodal-array in Albania (ANTICS—'AlbaNian TectonIcs of Continental

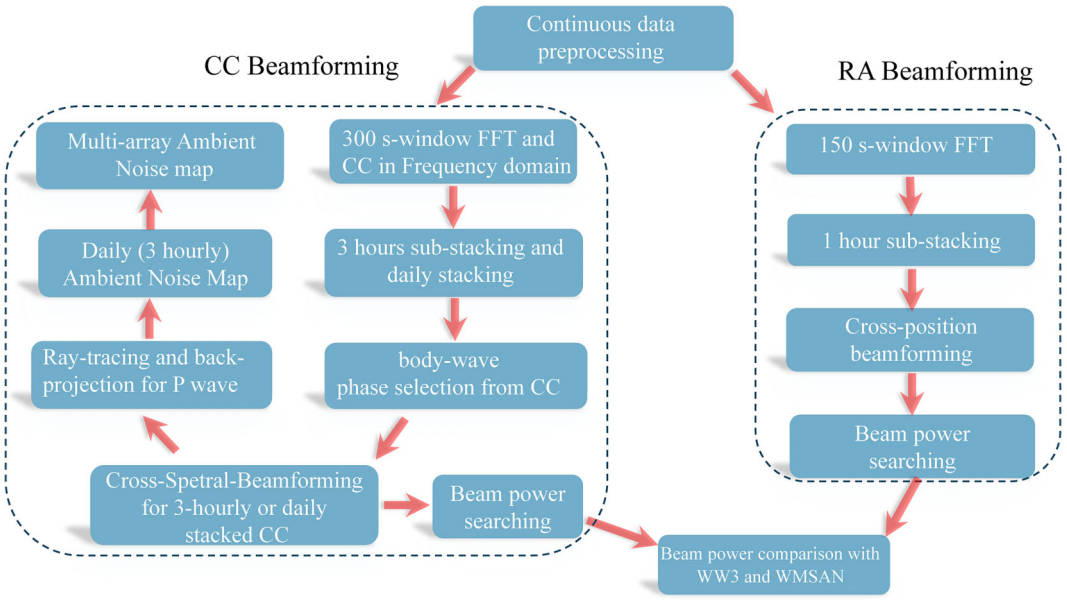

Figure 2. Workflow for retrieval of secondary microseisms from ambient noise CC beamforming and RA beamforming. CC beamforming is applied on three networks to jointly map the location of secondary microseisms and relative amplitude extraction for the geophones from ANTICS, whereas the RA beamforming is applied for the ANTICS broad-band stations to extract the absolute amplitude of secondary microseisms in the northern Atlantic.

Subduction', H. Agurto-Detzel *et al.* 2025a) which was operated jointly by the Karlsruhe Institute of Technology, Helmholtz Centre for Geosciences (GFZ) and Polytechnic University Tirana, Albania (PUT). ANTICS consisted of 332 4.5-Hz natural-frequency and 3-component geophones and 50 broad-band stations covering an area of 150 km by 150 km. These three networks provide sufficient data coverage and balanced sensitivity to reconstruct the microseism source map in the northern Atlantic and northern Pacific.

3 METHOD

We use a simple workflow for extracting the spatiotemporal variations of the secondary microseisms from the ambient noise CC beamforming for three seismic networks (G.G. Euler *et al.* 2014). We also retrieve temporal relative and absolute amplitude changes of secondary microseisms in the northern Atlantic. CC beamforming is applied to the time-series from 322 geophone stations of ANTICS, whereas the conventional sliding-window (150 s) RA beamforming is applied on the continuous velocity recordings from the 50 broad-band stations (F. Le Pape *et al.* 2021). The whole workflow for both methods is summarized in Fig. 2.

3.1 Data pre-processing and ambient noise cross-correlation

For broad-band stations (SCSN and the ANTICS broad-band subset), the instrument response is removed to obtain ground velocity, ensuring reliable amplitude scaling within the 0.1–0.2 Hz (5–10 s) microseism band used for absolute beam-power analysis (RA beamforming for the ANTICS broad-band subset). In contrast, the Hi-net short-period sensors and ANTICS nodal-array geophones have natural frequencies of 1 and 4.5 Hz, respectively. Deconvolving these responses to displacement or velocity at 0.1–0.2 Hz would amplify instrument noise and produce unstable long-period artefacts. Therefore, these data were kept in raw counts. Importantly, the short-period and nodal arrays are used only in CC beamforming, where amplitudes are normalized and the relative source localization, not absolute scaling, is the objective. Consequently, absolute amplitude comparisons are restricted to the broad-band networks. For the CC beamforming, we then cut the continuous seismic data into 300 s time segments (non-overlapping) and down-sample the data to 10 Hz. We use time–frequency domain whitening to remove the transient signals caused by earthquakes or other disturbances. Cross-correlations are calculated individually for all three networks (Figs 3a, c, e). In this work, we use Noisepy (C. Jiang & M.A. Denolle 2020) to adopt two-step spectral whitening that includes the running mean average (RMA) in the frequency domain (10 points in the frequency domain) and set the absolute amplitude of the complex Fourier spectrum to 1. The spectrally whitened continuous waveforms are then cross-correlated (see eq. 1) for station pairs in the Fourier domain. In the frequency domain, the cross-correlation can be written as:

$$R(x^i, x^j, \omega) = v(x^i, \omega) \cdot v^*(x^j, \omega), \tag{1}$$

where $v(x^i, \omega)$ are the pre-processed vertical time-series in the frequency domain recorded at location x_i and $*$ denotes the complex conjugate. The correlation function $R(x^i, x^j, \omega)$ is calculated for $i \neq j$, that is, all autocorrelations are excluded. Therefore, $n(n-1)/2$ unique station pairs are included.

3-hr stacks of cross-correlation traces ($\pm$ 150 s time lags are saved) for 36 segments are calculated to suppress transient signals and saved locally for further daily stacking and beamforming (Figs 3a, c, e).

3.2 CC Beamforming and RA beamforming

Different from conventional beamforming, CC beamforming (E. Ruigrok *et al.* 2017) requires that the data are first cross-correlated for all possible receiver pairs (see section above). The beam power,

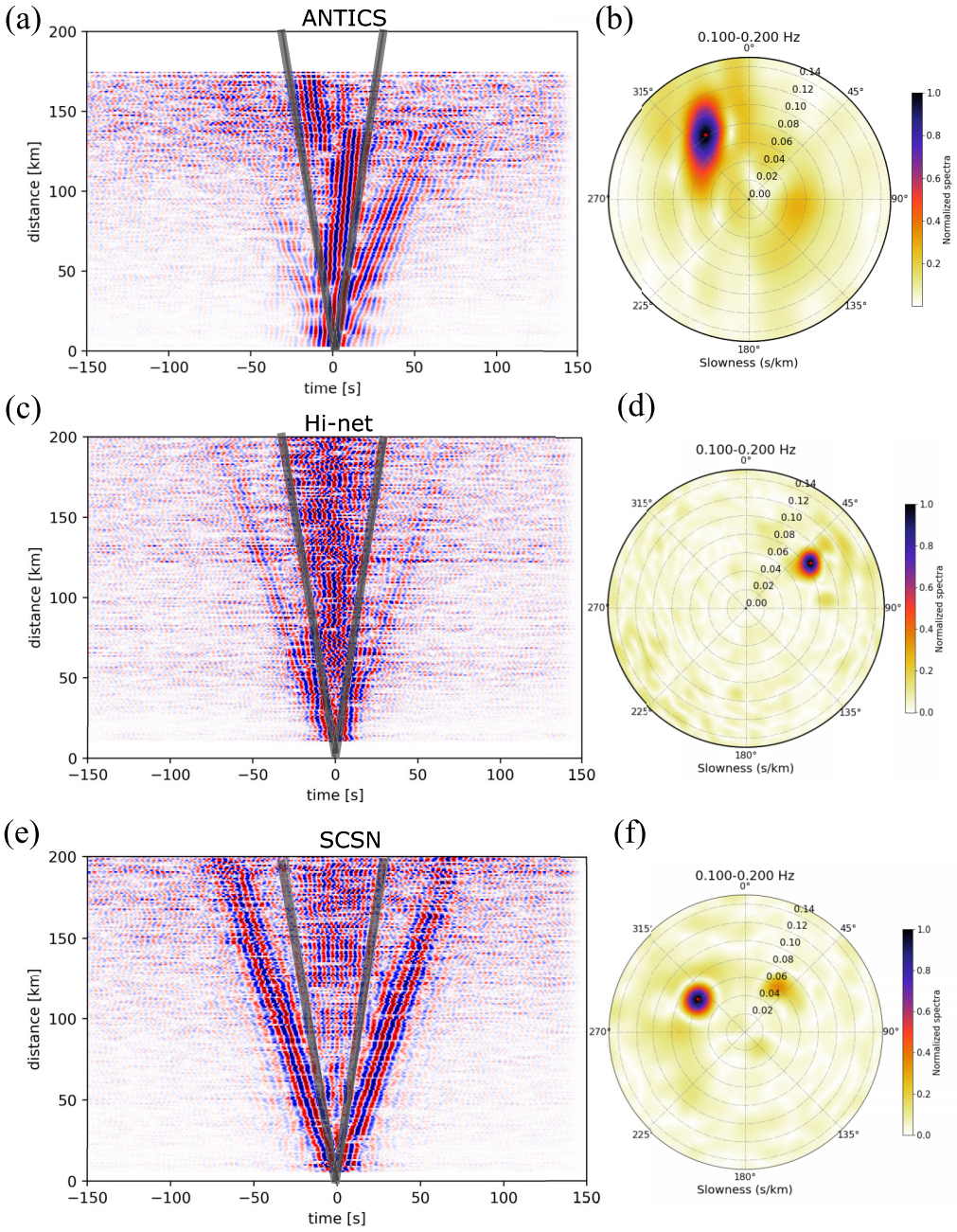

Figure 3. a,c,e: Ambient noise cross-correlation daily stacking for 2022 November 18 from three networks (filtered from 5 to 10 s); The thick grey dashed lines illustrate the reference velocity of 6.5 km s^{-1}. b,d,f: Beamforming of the cross-correlations shown on the left for the band 5–10 s. The outer limit of the circles corresponds to an apparent velocity of 6.5 km s^{-1}, as visualized by the grey line on the left.

therefore, can be expressed as:

$$B(p,\theta,\omega) = \left| \sum_{k=1}^{n(n-1)/2} R(\omega, x_k^i, x_k^j) \exp\left[I\omega d^k p \cos(\theta^k - \theta) \right] \right|. \quad (2)$$

Here d^k and θ^k denote the receiver–pair distance and azimuth, respectively. The k denotes the receiver–pair index. p and θ represents the slowness and backazimuth (baz), respectively, for frequency–wavenumber scanning. I denotes the imaginary unit.

The equation above provides a way to calculate beam power for cross-correlation waveforms. Before the beam power is calculated, the teleseismic *P* wave window in the cross-correlation waveforms has to be selected with an apparent velocity larger than 6.5 km s^{-1} to mute the Rayleigh waves (Figs 3a, c, e). The beam power for multiple frequency values is then averaged over the period range 5–10 s. Rayleigh waves dominate ambient noise in this frequency band but primarily represent local surface oscillations rather than the teleseismic body-wave microseisms targeted here (Figs 3b, d, f). Muting them enhances the coherence of the *P*-wave arrivals and prevents contamination from strong near-surface energy.

In contrast, the beam power from RA beamforming (K.D. Koper *et al.* 2009; M. Gal *et al.* 2015; K. Nishida & R. Takagi 2022) is

calculated directly from the velocity traces.

$$B(p,\theta,\omega)=\sum_{t=1}^{N}\left|\sum_{k=1}^{n}v_t(x^k,\omega)\exp\left[I\omega d^k p\cos(\theta^k-\theta)\right]\right|. \quad (3)$$

Here, d^k and θ^k denote the relative distance and azimuth with respect to the centre of the array, respectively. The k denotes the receiver index. The outer summation denotes the summation over N sliding time windows, with t the window index. Since the seismograms are analysed directly, we use a window length of 150 s to minimize contamination from transient earthquake signals and local disturbances, while still ensuring adequate frequency resolution in the 5–10 s band. Therefore, 24 segments are stacked hourly. The beam power for multiple frequency values is then averaged, as for CC beamforming over the period range 5–10 s.

3.3 Array response function

The array response function (ARF) describes how an array of sensors responds to a plane wavefield emanating from a particular direction or originating from a specific point source. The ARF encapsulates the phase and amplitude variations across the array elements, fundamentally influencing the beamforming output. Understanding the ARF is crucial for optimizing array configurations and beamforming algorithms to achieve the desired resolution and directivity characteristics. This subsection focuses on the comparative analysis of two prominent beamforming methods: RA beamforming and CC beamforming for three networks, respectively.

For the RA beamforming, the ARFs of the three networks display many small artefacts in the beam pattern image (Fig. A1), whereas the CC beamforming generates cleaner beam patterns and suffers less from non-coherent signals (Fig. A2). For HINET, the beam pattern from RA beamforming shows spurious secondary maxima for the 5 and 8-s beam patterns (Fig. A1). For ANTICS, due to the small aperture, the resolution deteriorates for lower frequencies and suffers from smearing in the slowness direction in the CC beamforming pattern (Fig. A2).

Quantitative resolution estimates from the array response functions (Figs A1–A2) demonstrate the differing capabilities of the three networks. The −3 dB (half-power) azimuthal beamwidths are approximately 20°–36° for ANTICS (depending on period), 12°–22° for SCSN, and 10°–18° for Hi-net at slowness 0.15 s km^{-1}. These values highlight how the smaller aperture of ANTICS leads to broader main lobes and reduced azimuthal resolution, whereas the large-aperture permanent arrays produce narrower beams. Nevertheless, the dense station spacing of ANTICS provides superior spatial coherence and sensitivity to short-wavelength, low-amplitude microseisms, particularly valuable in the Adriatic–Mediterranean region where local sources may dominate. The CC beamforming pattern (Fig. A2) also shows significantly reduced sidelobe energy relative to RA beamforming, confirming that CC beamforming enhances coherent body-wave retrieval and overall source-localization accuracy. These quantitative results underscore the complementary roles of dense nodal and sparse arrays in the multi-array analysis presented here.

3.4 Teleseismic *P* wave ray-tracing and backprojection

We use teleseismic *P*-phase energy to construct the beamforming and backprojection spectra. The direct *P* wave is the dominant phase within an epicentral distance of 25°–90°, corresponding to slowness values of 5–10 s deg^{-1} (G.G. Euler *et al.* 2014). This range captures coherent body-wave energy from the northern Atlantic and Pacific storms that reach our three northern Hemisphere arrays during winter.

The PP phase occupies a similar but partially overlapping slowness band (4.4–9.5 s deg^{-1}), yet its amplitude is generally smaller than that of the direct *P* wave for distances < 100° (including Pdiff). For larger distances (100°–125°), the PP phase may become stronger but shares comparable slowness (7–8 s deg^{-1}) with the *P* wave at 50°–65° epicentral distance (P. Gerstoft *et al.* 2008). To avoid ambiguity between these overlapping phases, we assume that only the direct *P* wave contributes significantly to the beam power within 25°–90°.

Other teleseismic phases such as Pdiff, PcP, PKPab–bc, PKiKP and PKIKP can also contribute energy to the beamforming spectrum. Among these, Pdiff (90°–110°) is back-projected as an extension of P. The PKPab and PKPbc branches form an arc in the slowness–distance domain (2–4.5 s deg^{-1} for 130°–152°), causing phase ambiguity; therefore, only PKPbc is considered. PKiKP and PKIKP are included to represent the farthest observable distances (> 152°).

3.5 Modelling ocean floor equivalent force

Based on the spectral density of the wave-induced pressure from the WW3 model (H. Tolman *et al.* 2014), we further inferred ambient noise source strength (equivalent vertical force F at the sea floor, Fig. 4h) in the secondary microseism band from 5 to 10 s. The equivalent vertical force F applied at the ocean floor is calculated by considering the amplification coefficients for the *P* wave (source site effects) following L. Retailleau & L. Gualtieri (2021) and L. Tomasetto *et al.* (2025). The amplification coefficient is related to the thickness of the ocean layer (bathymetry); therefore, we utilize a global bathymetry model at 30 arcmin resolution to match the same spatial resolution of the WW3 model (H. Tolman *et al.* 2014; L. Tomasetto *et al.* 2025).

The amplification coefficient can be expressed as below:

$$c_P(f,h)=\sqrt{\int_0^{\theta^*_{Pw}}\left|\frac{T_P(\theta_{Pw})}{1+R(\theta_{Pw})\exp\left(i\phi_w(h(r),2\pi f,\theta_{Pw})\right)}\right|^2 \mathrm{d}\theta_{Pw}}, \quad (4)$$

where f is the seismic frequency in Hz (twice the ocean wave frequency); h is the ocean depth in m; θ_{Pw} denotes the *P*-wave takeoff angle range; ϕ_w is the plane *P*-wave potential propagating in water; R is the seabed interface reflection coefficient and T_P is the seabed interface *P*-wave transmission coefficient.

The equivalent vertical force F could be expressed as:

$$F=2\pi\sqrt{\int_{-\pi/2}^{\pi/2}\int_0^{2\pi}\int_{f_{\min}}^{f_{\max}}c_P^2(\lambda,\phi,f_s)F_p R_E^2\cos\lambda\,\mathrm{d}\lambda\,\mathrm{d}\phi\,\mathrm{d}f}, \quad (5)$$

where F_p is the spectral density just below the sea surface in Pa^{2}m^{2}s from the WW3 model. $f_{\min}$ and $f_{\max}$ denote lower and upper frequency bounds in Hz. In this study, we only focus on the period band from 5 to 10 s (secondary microseism period band), therefore, $f_{\min}=0.1$ Hz and $f_{\max}=0.2$ Hz. R_E is the Earth's radius in m. λ and ϕ represent the latitude and longitude in degrees. For details on the computation, see L. Gualtieri *et al.* (2014) and L. Tomasetto *et al.* (2025).

3.6 Beam power estimation

To explore the relationship among the beam power of a single seismic array, significant wave height and the equivalent force of

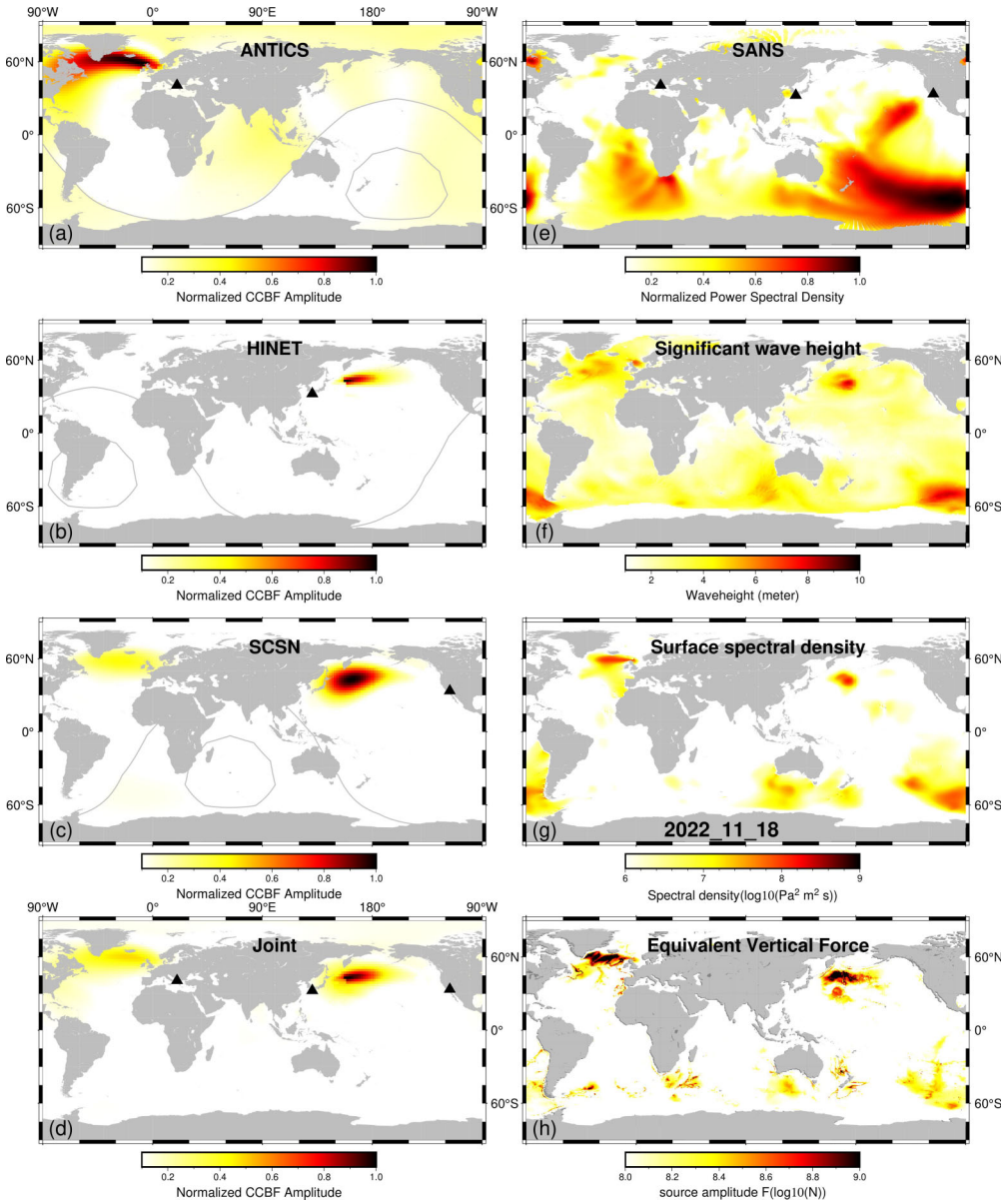

Figure 4. (a–c) Cross-correlation beam power and backprojection for three individual networks; grey curves in (a)–(c) denote epicentral distances of 90° and 120°. (d) Joint backprojection constraints from the three networks. (e) Seismic Ambient Noise Source (SANS) maps from full waveform inversion (J. Igel *et al.* 2021). (f) daily averaged wave height map on 2022 November 18 and (g) daily averaged surface spectral density at 5–10 s, as extracted from WW3 model. (h) Equivalent vertical force on the ocean floor considering the source site effects and assuming body wave propagation, reconstructed using WMSAN from L. Tomasetto *et al.* (2025).

the ocean floor, we utilize the ANTICS array to extract the temporal variation of beam power from the CC beamforming in the northern Atlantic. We search for the maximum beam power within the northwestern baz (270°–360°) and teleseismic *P* wave slowness (6–10 s deg^{-1}). We then compare the strength with the maximums of significant wave height from WW3 (F. Ardhuin *et al.* 2010), and the equivalent force for the *P* wave on the ocean floor (Fig. 5).

To extract the absolute beam power amplitude, we also applied the RA beamforming (Fig. 2) to the 50 broad-band seismometers of the ANTICS. As the nodal stations only have a corner frequency of 4.5 Hz and to minimize computational cost, we only try to extract the absolute beam power from the ANTICS broad-band stations and search for the maximum beam power in the northern Atlantic direction (the same search criterion as CC beamforming).

4 RESULTS AND DISCUSSION

4.1 Spatial and temporal variations of the secondary microseism locations

In this study, we focus on the continuous evolution of secondary microseisms extracted from joint ambient noise CC beamforming from the autumn of 2022 to the spring of 2023. We explore the robustness of monitoring secondary microseisms using three dense seismic arrays with different instrumentation for the Northern Hemisphere.

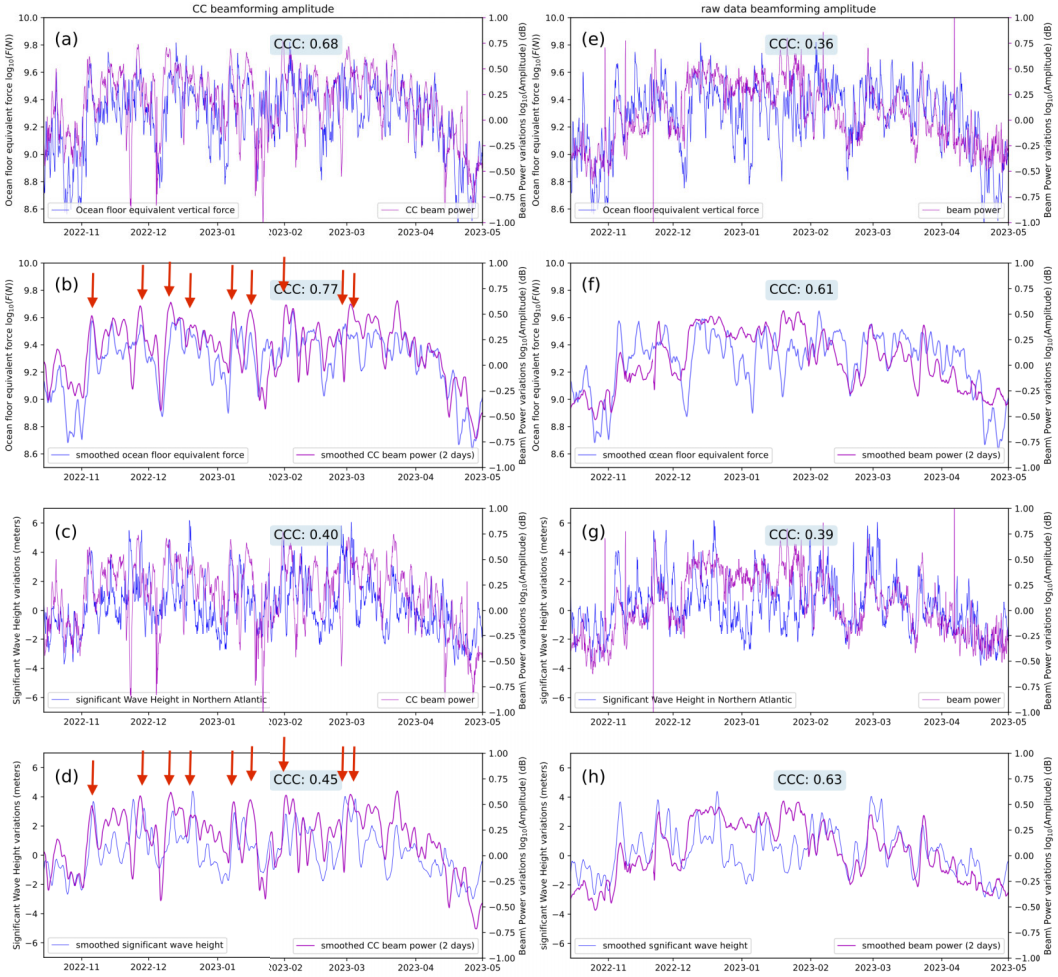

Figure 5. Comparison of beam power from CC beamforming (Left) and RA beamforming (Right) with ocean floor equivalent force and significant wave height for the northern Atlantic. (a) 3-hr maximum equivalent force and relative beam power retrieved from CC beamforming. (b) 2-d averaged maximum equivalent force and relative beam power (16 points median smoothing). (c) 3-hr significant wave height and relative beam power. (d) 2-d averaged maximum significant wave height and cc beam power (16 points median smoothing). (e) to (h) are equivalent comparisons of oceanographic variables with absolute beam power from RA beamforming. The red arrows in (b) and (d) denote significant storms in the northern Atlantic.

The high-density ANTICS nodal array (3 km interstation spacing) provides superior spatial coherence and enables robust beamforming even for short-wavelength (0.1–0.2 Hz) microseisms. Although its smaller aperture yields a broader −3 dB beamwidth (18° at 8s, see ARF in Figs A2 and A1) than Hi-net and SCSN (12°) and decreases the spatial resolution for multiple sources and low-frequency signals, the dense geometry enhances the signal-to-noise ratio and sensitivity to the microseism in the northern Atlantic and Mediterranean Sea. Conversely, the sparse wide-aperture permanent networks achieve finer azimuthal resolution but lower coherence for weak signals. The complementary combination of dense regional nodal arrays and large-aperture networks thus enables multiscale tracking of microseism sources across oceanic basins.

In the daily cross-correlations on 2022 November 18 for the ANTICS network (Fig. 3), the body wave signals with apparent velocities greater than 6.5 km s^{-1} are stronger than the surface waves and show significant amplitude differences between the left and right branches. For this case, the right branch shows stronger amplitudes at shorter interstation distance (0–130 km) than the left branch but at larger interstation distance (120–170 km), the left branch is much stronger (Fig. 3a). After applying CC-beamforming, ANTICS displays strong beam power around 315 ° in baz and 0.08 s km^{-1} (8.9 s deg^{-1}) in slowness, indicating that the dominant plane wave comes from the northwest, likely from the Atlantic.

On the same day, the cross-correlation body wave phases are rather weaker and more diffused on Hi-net and SCSN. For Hi-net, the left branch shows relatively stronger amplitudes than the right branch. The beamforming for Hi-net indicates that the dominant signal comes from the northeast. Meanwhile, SCSN displays a rather symmetric cross-correlation, and beamforming denotes that the dominant signal comes from the northwest and a weaker signal from the northeast. Considering the geographic location of Hi-net and SCSN, we can infer that the most influential signal for both networks comes from the same source. The dominant signal from the northwest in the ANTICS originates from another source, which likely corresponds to the weak signal with northeastern baz on the SCSN beam power plot.

Through the backprojection (Fig. 4), we can easily identify the locations of the microseisms. The contributing teleseismic energy

captured by ANTICS mainly comes from the northern Atlantic (Fig. 4a). The wave height map and surface spectral density from the WW3 model (F. Ardhuin *et al.* 2010) shows two groups of storms between North America and Europe on this day (Figs 4f–g), one located in the northern Atlantic covering a large area and another spatially concentrated one in the North Sea. At the same time, the SCSN backprojection also captured the same ambient noise source (Fig. 4c) within the northern Atlantic covering a similar area as determined by ANTICS. For the northern Pacific, ANTICS only reveals very weak beam power, presumably because of the large distance from the source to ANTICS. SCSN and Hi-net detect the same strong and focused ambient noise source south of the Kamchatka Peninsula and east of Japan. Due to the larger distance to SCSN, the beam power is spread over a wider area than in the Hi-net stack (Fig. 4b). We normalized, linearly summed and then averaged the beam powers for the three networks to stabilize the result and improve the resolution. The joint observations (Fig. 4d) provide higher consistency with the significant ocean wave height (Fig. 4f) and surface spectral density (Fig. 4g) compared to the single-array beamformings. Fig. 4(e) shows the global daily ambient noise map from Rayleigh wave FWI (SANS J. Igel *et al.* 2021) for comparison, which exhibits higher lateral smearing.

However, the significant wave height and WW3 ocean surface spectral density only reflect the ocean weather near the open ocean surface without consideration of the transmission to the crust and the effect of bathymetry as an amplification coefficient; in other words, neither directly represents the distribution of the physics of secondary microseism generation. To account for this physical mechanism and the ocean–solid Earth coupling, we apply a further modulation of the WW3 spectra using the WMSAN (L. Tomasetto *et al.* 2025). This converts the surface spectral density into a proxy for the equivalent vertical force (P wave) at the seafloor by integrating the nonlinear pressure spectral density and including bathymetry-dependent amplification coefficients for body waves. The resulting model (Fig. 4h) represents the effective ocean floor forcing responsible for P wave secondary microseisms and better reproduces the observed beam-power amplitude and timing. The modelled sources are mainly located in the northern Atlantic and northern Pacific with reduced contributions from the Southern Hemisphere (Fig. 4h) compared to the wave height map (Fig. 4f) and the surface spectral density (Fig. 4g), therefore, the modelled sources are more consistent with our observation than surface spectral density and wave height. During our study period (autumn 2022–spring 2023), Northern Hemisphere storm systems dominate secondary microseism generation. In contrast, Southern Hemisphere sources are not detected, which we attribute to both seasonal variability and array distribution. The austral summer months produce relatively weaker microseisms around Antarctica compared to the intense boreal winter storms in the northern Atlantic and northern Pacific (P. Gerstoft *et al.* 2008; L. Li *et al.* 2020). In addition, all three arrays used here are located in the Northern Hemisphere, making them far less sensitive to Antarctic sources, which would need to propagate over distances exceeding 120°–150°. At such path lengths, attenuation and interference between different seismic phases in the 5–10 s band further reduce detectability (L. Retailleau & L. Gualtieri 2021). This explains why Southern Hemisphere contributions are negligible in our observations.

To further retrieve the temporal variations, we directly compute our 3-hr substacks of the cross-correlations for the whole period and repeat the beamforming and backprojection process for the whole data set. On the same day of 2022 November 18, the microseism in the northern Atlantic expanded westward progressively from the west coast of Great Britain and Ireland to the east coast of Canada (Figs A3a–c). The surface spectral density from the WW3 model also displays a similar pattern (Figs A3g–i). However, we should note that a new oceanic storm was generating near the east coast of Canada, which is more obvious in the significant wave height map (Figs A3e–f), leading to a gradually broader microseism zone in the northern Atlantic with roughly 3 hr delay relative to the significant wave height (Figs A3a–f). On 2022 November 19 the new oceanic storm near Canada became stronger, migrated eastwards very quickly (Figs A4d–f) and dominated the northern Atlantic on 2022 November 20 (Figs A5d–f), leading to the significantly high microseism amplitudes on 2022 November 20 (Figs A5a–c, j–l). In contrast, the microseism in the northern Pacific was generated by a unique storm system and was moving eastward very slowly, then separated into two small storm systems (Figs A4d–f) and gradually died out on 2022 November 20 (Figs A5a–c). This temporal correspondence suggests that the nonlinear coupling between opposing wave systems strengthens during the mature stage of storm evolution, constraining the development timescale of wind-wave systems to roughly the period over which microseism amplitudes rise to their maximum. A complete spatiotemporal evolution of the secondary microseism generation from 2022 October 1 to 2023 May 1 is visualized in the supplementary video.

In summary, these exemplary comparisons demonstrate that our CC beamforming using multiple arrays can capture and constrain the spatiotemporal evolution of secondary microseisms with unprecedented resolution, at least in the Northern Hemisphere. The multi-array approach can significantly reduce the smearing effects of a single array and avoids the interferences caused by other seismic phases. The direct comparison with WMSAN equivalent-force modelling links the predicted nonlinear ocean-solid earth coupling from wave models to higher resolution real observations.

4.2 Temporal strength variations of secondary microseism in the northern Atlantic

Because different data types and beamforming methods can yield different representations of microseism sources, we next evaluate how well each approach and each sub-data set of ANTICS (nodal-geophone and broad-band seismometer) captures the strength of the secondary microseism L. Retailleau *et al.* (2018) and compare the results with modelled equivalent-force variations in the northern Atlantic derived from WMSAN. This comparison tests the physical consistency between observed seismic power at a specific baz direction range and the nonlinear ocean–wave interactions that generate secondary microseisms. It clarifies the advantages and limitations of the CC and RA beamforming methods.

Based on the two types of data sets from ANTICS and two different beamforming methods, the relative and absolute amplitudes of secondary microseisms in the northern Atlantic are retrieved through a grid-search to find the local maximum (northern Atlantic direction) in the beam power patterns. In order to obtain stable estimate, the rolling median within a 6-hr time window is taken to represent the microseism strength in that time window. First, outliers, which are mostly related to large amplitudes, from teleseismic or local earthquakes, are removed. Outliers are identified using the 10th and 90th percentiles of the distribution: the interpercentile range (IPR = Q90–Q10) is taken as a robust measure of variability. Any value lying outside (Q10-IPR, Q90+IPR), that is, a range corresponding to three times the IPR(10–90), is considered an outlier and removed (Fig. A6). The resulting gaps are closed by

forward-filling before calculating the 6 hr rolling mean. Finally, a longer rolling mean (48 samples) is applied to the cleaned series to highlight two-day trends (Fig. 5). For example, the destructive Turkey-Syria earthquake (M_w 7.8) caused significant ground motion in Albania, but the IPR pre-processing and further smoothing can alleviate the influence on the beam power from the outliers caused by strong earthquakes (Fig. A6). This approach is comparable to the traditional IQR method (based on quartiles), but using Q10–Q90 provides a wider, more permissive band that reduces false positives in skewed data, where several apparent spikes represent valid signals due to strong storm activity. The procedure preserves the underlying microseism variability while reliably discarding short-lived extreme excursions caused by seismic activity.

Figs 5(a) and (e) compare the 3-hr ocean floor equivalent force with the beam power calculated from CC beamforming and RA beamforming. (c) and (g) are the 3-hr comparisons between the beam power and maximum wave height. The two beam power data sets, ocean floor equivalent force and significant wave height time-series are smoothed through a rolling mean with a window size of 48 hr to retrieve the long-period trends (Figs 5b, f, d, h).

The beam power from CC beamforming shows a higher correlation with the modelled equivalent force (CCC = 0.77) than does RA beamforming for the northern Atlantic (CCC = 0.61). Several quiet intervals in the northern Atlantic during the boreal winter (late December–early January and late January–early February) are reproduced more faithfully by the CC beamforming results (Figs 5b and f), indicating that CC better suppresses incoherent local or regional noise. In contrast, the lower correlation between broad-band RA beam power and the modelled equivalent force (and wave height) during winter likely reflects elevated noise from local Mediterranean sources. Figs A7–A8 support this interpretation: coastal ANTICS stations exhibit PSD levels up to 15 dB higher than inland stations in the 0.1–0.2 Hz band (up to 30 dB for 0.2–1 Hz) and the enhanced modelled equivalent force near the central Mediterranean Sea and Ionian Sea, demonstrating that local bathymetry, shallow-water resonance and wind-sea activity increase incoherent energy in this frequency and slowness range. These local contributions primarily affect RA beamforming, whereas CC beamforming—by focusing on coherent body-wave arrivals—more accurately tracks open-ocean (Atlantic) forcing. Similar conclusions were drawn by A.M. Borzì *et al.* (2025), which showed that Mediterranean microseism amplitudes correlate most strongly with local wave heights within 500 km of the coast and peak during winter when wind-driven sea waves dominate.

In summary, the strong temporal agreement between the CC beam power and the modelled equivalent force confirms that CC beamforming effectively isolates coherent body-wave microseism energy generated by nonlinear ocean–wave interactions in the northern Atlantic, separating it from near-field noise. The weaker RA correlation reflects additional incoherent local energy, particularly from the Mediterranean. This comparison validates the physical basis of the WMSAN framework and underscores the potential of multi-array CC analysis for identifying global storm-driven body-wave sources. On the other hand, the complementary performance of CC and RA beamforming indicates that both approaches are valuable for continuous monitoring: CC isolates coherent far-field body-wave energy that best traces large-scale storm activity, whereas RA beamforming, together with PPSD analysis, preserves absolute amplitude information useful for assessing local variability and near-field sources with different dominant frequency (Fig. A7, A8, A9). The dense ANTICS nodal array demonstrates that compact, low-cost deployments can capture these processes with high spatial coherence, though their broad beamwidth limits azimuthal resolution compared with large-aperture networks. Consequently, the current multi-array configuration markedly improves spatial resolution for Northern Hemisphere storm monitoring compared with single-array analyses, and future global extensions will benefit from arrays of differing apertures to reduce directional bias and enhance period-dependent coverage of secondary microseisms.

Beyond demonstrating methodological robustness, these results highlight that coherent body-wave microseisms can serve as quantitative indicators of storm evolution and ocean–seafloor coupling strength. The strong match between modelled forcing and observed CC beamforming amplitudes suggests that dense seismic networks can operate as cost-effective, physics-based sensors for large-scale ocean monitoring and for improving coupled atmosphere–ocean–solid-Earth models. The temporal evolution described above shows that secondary microseisms reach their maximum strength during the mature stage of North Atlantic storms, when opposing wave systems become established. This pattern implies that nonlinear coupling between wind-generated waves develops progressively as storms intensify. For detailed investigations of shorter period microseisms, especially in nearby seas such as the Mediterranean or Ionian, future studies should incorporate three-component polarization filtering or wavefield-matching methods. In addition, advanced numerical 3-D acoustic–seismic modelling and inversion should be considered to better capture the influence of local bathymetry and crustal heterogeneity, particularly near deep trenches and beneath the arrays.

5 CONCLUSION

In this study, we propose a new workflow based on ambient noise CC beamforming to track the sources of secondary microseism in the Northern Hemisphere. We applied this technique to three differently instrumented networks (ANTICS; SCSN and Hi-net) for the time period from fall 2022 to spring 2023. The teleseismic *P* phases in the cross-correlation traces are selected by slowness range and used for the beamforming and backprojection. The distribution of the secondary microseism sources retrieved from our joint beamforming-backprojection has an excellent correlation with the location of the sea floor equivalent forces predicted by the WW3-WMSAN model, considering the source site effect and bathymetry. The winter oceanic storms in the northern Atlantic and Pacific prevail over the secondary microseism of the whole Northern Hemisphere. The beam power extracted from the beamforming of the ANTICS data shows that we can predict not only the location but also the excitation strengths of the microseism source area. We also note that such results can be achieved with inexpensive seismic nodal stations that are normally only used for local seismicity (P.M. Shearer *et al.* 2023) and structural ambient noise studies (F. Cheng *et al.* 2021). More detailed storm evolution analysis, including their waxing and waning stages and how they relate to the generation efficiency of microseisms, will be expanded in our future work.

ACKNOWLEDGMENTS

We thank Prof. Joachim Ritter, Prof. Frank Krueger, Thomas Forbriger, Han Xiao, Fabrice Ardhuin and Jonas Igel for helpful discussions. Editor Sidao Ni, reviwer Qiaoxia Liu and Chris Carchedi

helped to enhance the clarity of presentation and depth of discussion. The authors gratefully acknowledge the Earth System Modelling Project (ESM) for funding this work by providing computing time on the ESM partition of the supercomputer JUWELS Jülich Supercomputing Centre (2021) at the Jülich Supercomputing Centre (JSC). The authors also acknowledge that open-source visualization and computation Python packages Noisepy, Numpy, SciPy, Matplotlib, Obspy and PyGMT are heavily used to produce the figures in this paper.

SUPPORTING INFORMATION

Supplementary data are available at *GJIRAS* online.

output_small.mp4.zip

Please note: Oxford University Press are not responsible for the content or functionality of any supporting materials supplied by the authors. Any queries (other than missing material) should be directed to the corresponding author for the article.

DATA AVAILABILITY

The ANTICS data set (H. Agurto-Detzel *et al.* 2025b) will be openly available at the GEOFON web service (https://geofon.gfz.de/) from May 2028 (Network code: X3). The raw waveform of Hi-net was downloaded from https://www.Hi-net.bosai.go.jp and the raw waveform data of SCSN were downloaded from EarthScope Consortium Data Services. The cross-correlations for three networks are computed using Noisepy and cross-correlation data could be accessed on request. The cross-correlation beamforming and backprojection code and data are published at RADAR4KIT (Gao & Rietbrock 2025). The significant wave height is retrieved from https://data.marine.copernicus.eu/ and the power spectral distribution is accessed from the output of the ocean wave WW3 model at ftp://ftp.ifremer.fr/ifremer/ww3/HINDCAST/SISMO/. The ocean floor equivalent force is calculated based on WW3 model using the Wave Model Sources of Ambient Noise (WMSAN) code retrieved from https://tomasetl.gricad-pages.univ-grenoble-alpes.fr/ww3-source-maps.

REFERENCES

Agurto-Detzel, H. *et al.*, 2025a. The ANTICS large-N seismic deployment in Albania, *Ann. Geophys.,* **68**.

Agurto-Detzel, H. *et al.*, 2025b. AlbaNian TectonIcs of Continental Subduction (ANTICS). GFZ Data Services. doi: 10.35097/d7zbw6eudy728tp3.

Ardhuin, F. & Roland, A., 2012. Coastal wave reflection, directional spread, and seismoacoustic noise sources, *J. geophys. Res.: Oceans,* **117**(C11).

Ardhuin, F. *et al.*, 2010. Semiempirical dissipation source functions for ocean waves. Part i: definition, calibration, and validation, *J. Phys. Oceanogr.,* **40,** 1917–1941.

Ardhuin, F., Stutzmann, E., Schimmel, M. & Mangeney, A., 2011. Ocean wave sources of seismic noise, *J. geophys. Res.,* **116,** C006952.

Ardhuin, F., Gualtieri, L. & Stutzmann, E., 2015. How ocean waves rock the earth: two mechanisms explain microseisms with periods 3 to 300 s, *Geophys. Res. Lett.,* **42**(3), 765–772.

Borzì, A.M., Cannata, A., Panzera, F., D'Amico, S., Re, C.L. & Aster, R.C., 2025. Microseism amplitude and wave power in the Mediterranean Sea (1996–2023), *J. geophys. Res.: Solid Earth,* **130**.

Boué, P. & Tomasetto, L., 2023. Opportune detections of global *P*-wave propagation from microseisms interferometry, *C. R. Géosci.,* **355,** 1–16.

Boué, P., Poli, P., Campillo, M., Pedersen, H., Briand, X. & Roux, P., 2013. Teleseismic correlations of ambient noise for deep global imaging of the Earth, *Geophys. J. Int.,* **194,** 844–848.

Boué, P., Poli, P., Campillo, M. & Roux, P., 2014. Reverberations, coda waves and ambient noise: correlations at the global scale and retrieval of the deep phases, *Earth planet. Sci. Lett.,* **391,** 137–145.

Bromirski, P.D. *et al.*, 2017. Tsunami and infragravity waves impacting Antarctic ice shelves, *J. geophys. Res.: Oceans,* **122**(7), 5786–5801.

California Institute of Technology (Caltech), 1926. Southern California Seismic Network, International Federation of Digital Seismograph Networks. Other/Seismic Network. doi: 10.7914/SN/CI.

Cheng, F. *et al.*, 2021. High-Resolution Ambient Noise Imaging of Geothermal Reservoir Using 3C Dense Seismic Nodal Array and Ultra-Short Observation, *J. geophys. Res.: Solid Earth,* **126**(8), e2021JB021827.

Chevrot, S., Sylvander, M., Benahmed, S., Ponsolles, C., Lefèvre, J.M. & Paradis, D., 2007. Source locations of secondary microseisms in western Europe: evidence for both coastal and pelagic sources, *J. geophys. Res.: Solid Earth,* **112**(B11).

Euler, G.G., Wiens, D.A. & Nyblade, A.A., 2014. Evidence for bathymetric control on the distribution of body wave microseism sources from temporary seismic arrays in Africa, *Geophys. J. Int.,* **197,** 1869–1883.

Farra, V., Stutzmann, E., Gualtieri, L., Schimmel, M. & Ardhuin, F., 2016. Ray-theoretical modeling of secondary microseism *P* waves, *Geophys. J. Int.,* **206,** 1730–1739.

Gal, M., Reading, A.M., Ellingsen, S.P., Gualtieri, L., Koper, K.D., Burlacu, R., Tkalčïïc, H. & Hemer, M.A., 2015. The frequency dependence and locations of short-period microseisms generated in the Southern Ocean and West Pacific, *J. geophys. Res.: Solid Earth,* **120,** 5764–5781.

Gao, Y. & Rietbrock, A., 2025. High-resolution spatiotemporal monitoring of secondary microseisms via multi-array analysis [Dataset]. RADAR4KIT. doi: 10.35097/hr1xtyxjwu1fyfs7.

Gerstoft, P., Shearer, P.M., Harmon, N. & Zhang, J., 2008. Global P, PP, and PKP wave microseisms observed from distant storms, *Geophys. Res. Lett.,* **35**(23).

Gualtieri, L., Stutzmann, E., Capdeville, Y., Ardhuin, F., M. Schimmel, A.M. & Morelli, A., 2013. Modeling secondary microseismic noise by normal mode summation, *Geophys. J. Int.,* **193,** 1732–1745.

Gualtieri, L., Stutzmann, E., Farra, V., Capdeville, Y., Schimmel, M., Ardhuin, F. & Morelli, A., 2014. Modelling the ocean site effect on seismic noise body waves, *Geophys. J. Int.,* **197,** 1096–1106.

Gualtieri, L., Stutzmann, E., Capdeville, Y., Farra, V., Mangeney, A. & Morelli, A., 2015. On the shaping factors of the secondary microseismic wavefield, *J. geophys. Res.: Solid Earth,* **120,** 6241–6262.

Gualtieri, L., Bachmann, E., Simons, F.J. & Tromp, J., 2020. The origin of secondary microseism Love waves, *Proc. Natl Acad. Sci.,* **117**(47), 29 504–29 511.

Hasselmann, K., 1963. A statistical analysis of the generation of microseisms, *Rev. Geophys.,* **1**(2), 177–210.

Igel, J., Ermert, L. & Fichtner, A., 2021. Rapid finite-frequency microseismic noise source inversion at regional to global scales, *Geophys. J. Int.,* **227,** 169–183.

Jiang, C. & Denolle, M.A., 2020. Noisepy: a new high-performance python tool for ambient-noise seismology, *Seismol. Res. Lett.,* **91,** 1853–1866.

Jülich Supercomputing Centre, 2021. JUWELS Cluster and Booster: Exascale Pathfinder with Modular Supercomputing Architecture at Juelich Supercomputing Centre, *J. Large-Scale Res. Facilities,* **7**(A138).

Kedar, S., Longuet-Higgins, M., Webb, F., Graham, N., Clayton, R. & Jones, C., 2008. The origin of deep ocean microseisms in the North Atlantic Ocean, *Proc. R. Soc. A: Math. Phys. Eng. Sci.,* **464,** 777–793.

Koper, K.D. & Hawley, V.L., 2010. Frequency dependent polarization analysis of ambient seismic noise recorded at a broadband seismometer in the central United States, *Earthq. Sci.,* **23,** 439–447.

Koper, K.D., de Foy, B. & Benz, H., 2009. Composition and variation of noise recorded at the yellowknife seismic array, 1991–2007, *J. geophys. Res.: Solid Earth,* **114**(B10).

Le Pape, F., Craig, D. & Bean, C., 2021. How deep ocean-land coupling controls the generation of secondary microseism Love waves, *Nat. Commun.,* **12**.

Lecocq, T., Hicks, S.P., Noten, K.V. & et al., 2020. Global quieting of high-frequency seismic noise due to COVID-19 pandemic lockdown measures, *Science,* **369**(6509), 1338–1343.

Li, L., Boué, P., Retailleau, L. & Campillo, M., 2020. Spatiotemporal correlation analysis of noise-derived seismic body waves with ocean wave climate and microseism sources, *Geochem. Geophys. Geosyst.,* **21**(9), e2020GC009112.

Liu, Q. *et al.*, 2016. Source locations of teleseismic *P*, *SV*, and *SH* waves observed in microseisms recorded by a large aperture seismic array in China, *Earth planet. Sci. Lett.,* **449,** 39–47.

Liu, Q., Ni, S., Qiu, Y., Zeng, X., Zhang, B., Wang, F., Duan, Y. & Xu, Z., 2020. Observation of teleseismic *S* wave microseisms generated by typhoons in the western Pacific Ocean, *Geophys. Res. Lett.,* **47**(19), e2020GL089031.

Liu, Q., Zhou, Y., Ni, S., Xu, M., Qiu, Y., Zhang, Y., Yu, C. & Chu, R., 2024. Resolvability of multiple microseismic *P*-wave source regions with two large seismic arrays in China and the United States, *Seismol. Res. Lett.,* **95**(3), 1885–1898.

Longuet-Higgins, M.S., 1950. A theory of the origin of microseisms, *Phil. Trans. R. Soc. Lond. Ser. A, Math. Phys. Sci.,* **243**(857), 1–35.

Lu, Y., Pedersen, H.A., Stehly, L. & Group, A.W., 2021. Mapping the seismic noise field in Europe: spatio-temporal variations in wavefield composition and noise source contributions, *Geophys. J. Int.,* **228**(1), 171–192.

Lu, Y., Schmid, S.M., Wang, Q.Y. & Bokelmann, G., 2023. Mapping the mantle transition zone discontinuities across South-central Europe using body waves from seismic noise correlations, *Earth planet. Sci. Lett.,* **624,** 118457.

McNamara, D.E. & Boaz, R.I., 2019. Visualization of the seismic ambient noise spectrum, in *Seismic Ambient Noise,* pp. 1–29, Nakata, N., Gualtieri, L. & Fichtner, A., (eds), Cambridge Univ. Press.

Nakata, N., Gualtieri, L. & Fichtner, A., 2019. *Seismic Ambient Noise,* Cambridge Univ. Press.

Nishida, K. & Takagi, R., 2016. Teleseismic wave microseisms, *Science,* **353**(6302), 919–921.

Nishida, K. & Takagi, R., 2022. A global centroid single force catalog of *P*-wave microseisms, *J. geophys. Res.: Solid Earth,* **127**.

Obara, K., Kasahara, K., Hori, S. & Okada, Y., 2005. A densely distributed high-sensitivity seismograph network in Japan:Hi-net by National Research Institute for Earth Science and Disaster Prevention, *Rev. Sci. Instrum.,* **76,** 021301–021301.

Obrebski, M.J., Ardhuin, F., Stutzmann, E. & Schimmel, M., 2012. How moderate sea states can generate loud seismic noise in the deep ocean, *Geophys. Res. Lett.,* **39**(11).

Okada, Y., Kasahara, K., Hori, S., Obara, K., Sekiguchi, S., Fujiwara, H. & Yamamoto, A., 2004. Recent progress of seismic observation networks in Japan—Hi-net, F-net, K-NET and KiK-net, *Earth Planets Space,* **56,** 15–28.

Pedersen, H.A., Mattern, F., Poli, P. & Stehly, L., 2022. Imaging with seismic noise: improving extraction of body wave phases from the deep Earth through selective stacking based on H/V ratios, *Geophys. J. Int.,* **232**(2), 1455–1467.

Peterson, J., 1993. *Observations and Modeling of Seismic Background Noise,* USGS Open File Report 93-322, U.S. Geological Survey, 94 pp.

Poli, P., Campillo, M., Pedersen, H. & LAPNET Working Group, 2012. Body-wave imaging of Earth's mantle discontinuities from ambient seismic noise, *Science,* **38,** 1063–1065.

Retailleau, L. & Gualtieri, L., 2021. Multi-phase seismic source imprint of tropical cyclones, *Nat. Commun.,* **12**(1), 2064.

Retailleau, L., Landès, M., Gualtieri, L., Shapiro, N.M., Campillo, M., Roux, P. & Guilbert, J., 2018. Detection and analysis of a transient energy burst with beamforming of multiple teleseismic phases, *Geophys. J. Int.,* **212,** 14–24.

Ruigrok, E., Gibbons, S. & Wapenaar, K., 2017. Cross-correlation beamforming, *J. Seismol.,* **21,** 495–508.

Sager, K., Boehm, C., Ermert, L., Krischer, L. & Fichtner, A., 2018. Sensitivity of seismic noise correlation functions to global noise sources, *J. geophys. Res.,* **123,** 6911–6921.

Shapiro, N.M., Campillo, M., Stehly, L. & Ritzwoller, M., 2005. High resolution surface wave tomography from ambient seismic noise, *Science,* **307,** 1615–1618.

Shearer, P.M., Meng, H. & Fan, W., 2023. Earthquake detection using a nodal array on the San Jacinto Fault in California: evidence for high foreshock rates preceding many events, *J. geophys. Res.: Solid Earth,* **128**(3), e2022JB025279.

Shen, W., Ritzwoller, M.H. & Schulte-Pelkum, V., 2013. Crustal and uppermost mantle structure in the central U.S. encompassing the Midcontinent Rift, *J. geophys. Res.,* **118,** 4325–4344.

Stutzmann, E., Ardhuin, F., Schimmel, M., Mangeney, A. & Patau, G., 2012. Modelling long-term seismic noise in various environments, *Geophys. J. Int.,* **191,** 707–722.

Tanimoto, T. & Anderson, A., 2023. Seismic noise between 0.003 Hz and 1.0 Hz and its classification, *Prog. Earth Planet Sci.,* **10,** 1–22.

Tolman, H. *et al.*, 2014. *User Manual and System Documentation of WAVEWATCH III version 4.18,* NOAA/NWS/NCEP. Available at: https://polar.ncep.noaa.gov/waves/wavewatch/manual.v4.18.pdf

Tomasetto, L., Boué, P., Ardhuin, F., Stutzmann, E., Xu, Z., De Plaen, R. & Stehly, L., 2025. WMSAN Python Package: From Oceanic Forcing to Synthetic Cross-correlations of Microseismic Noise, *Seismica,* **4**.

Xiao, H., Tanimoto, T. & Xue, M., 2021. Study of *S*-wave microseisms generated by storms in the southeast Australia and North Atlantic, *Geophys. Res. Lett.,* **48**.

APPENDIX A: SUPPLEMENTARY FIGURES

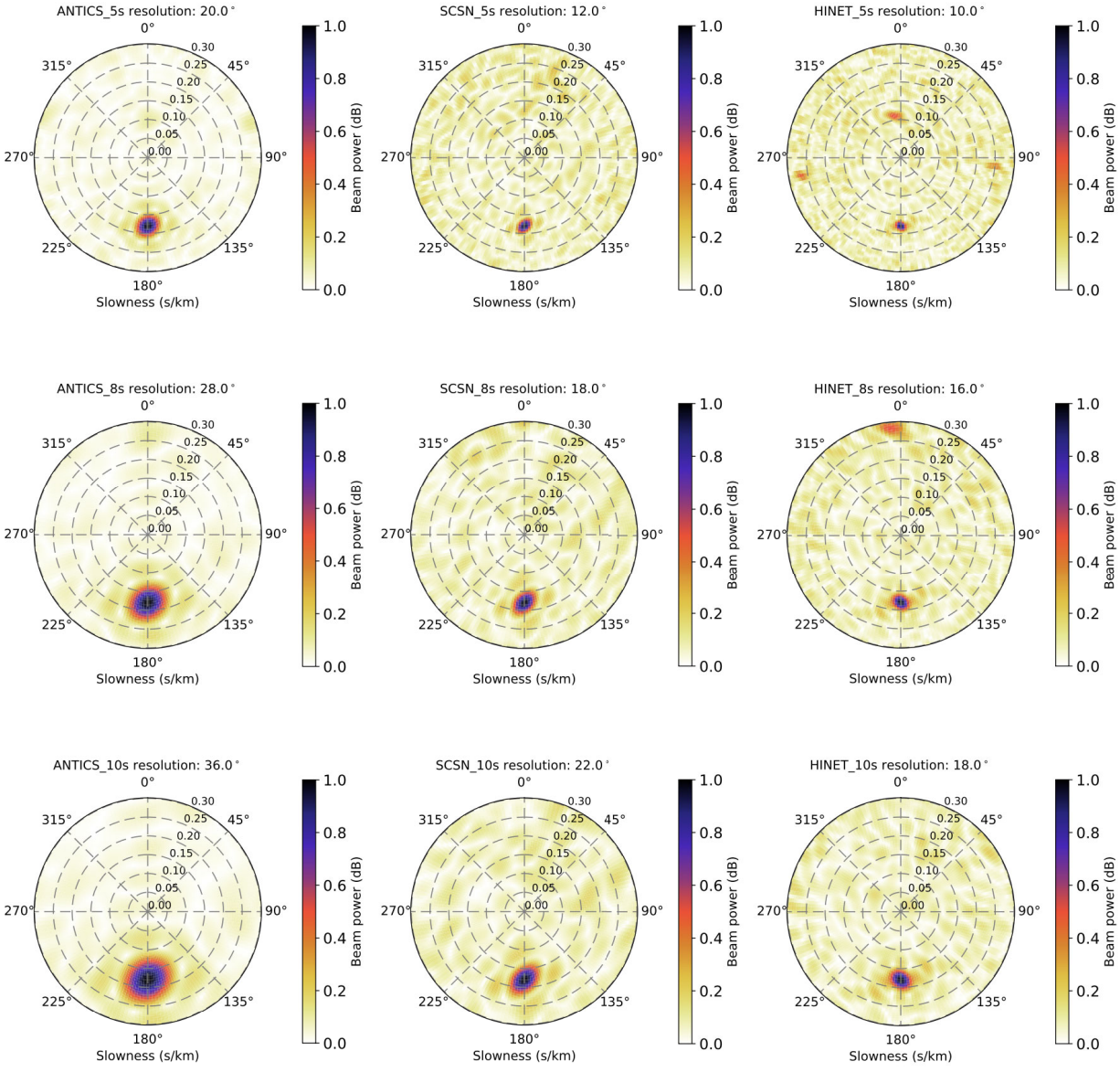

Figure A1. RA beamforming array response for a plane wave with slowness 0.15 s km^{-1} at 180° backazimuth. The header lines provide the −3 db (half-power) azimuthal beam widths as an estimate of backazimuth resolution.

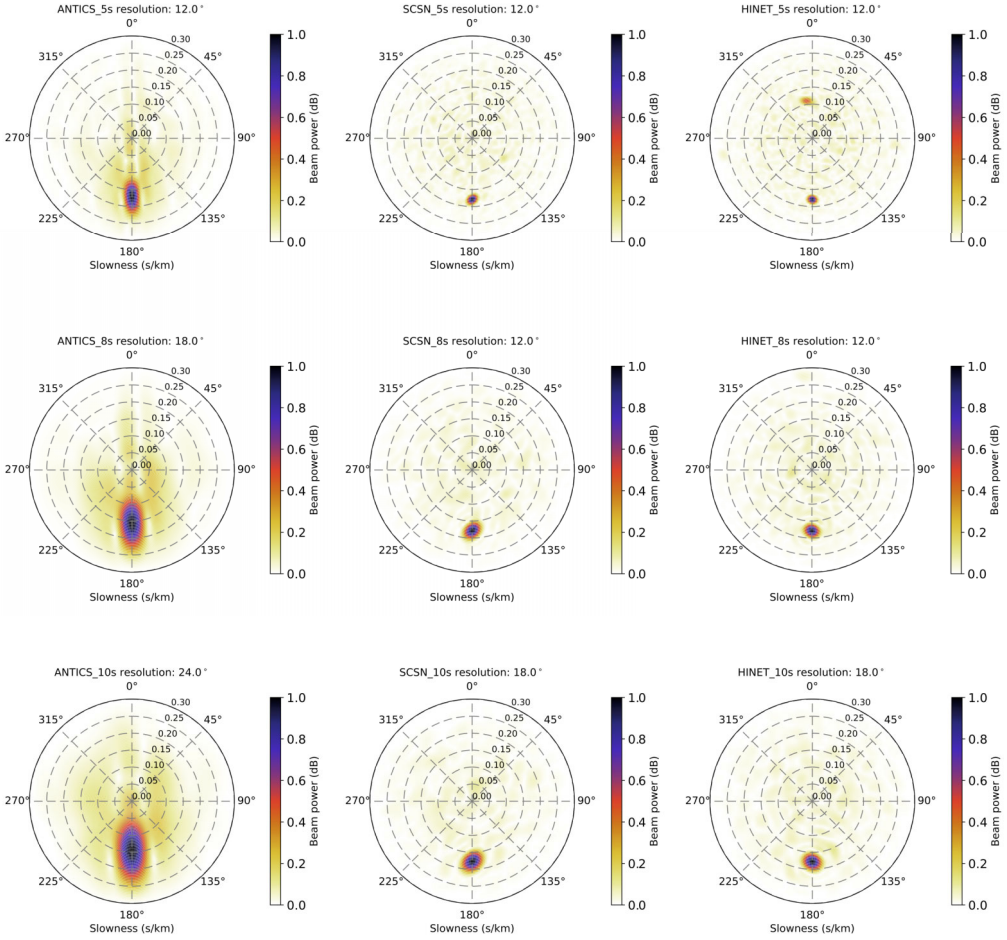

Figure A2. Three network cross-correlation beamforming array response functions for a plane wave coming with slowness 0.15 s km^{-1} at 180° backazimuth. The header lines provide the −3 db (half-power) azimuthal beam widths as an estimate of backazimuth resolution.

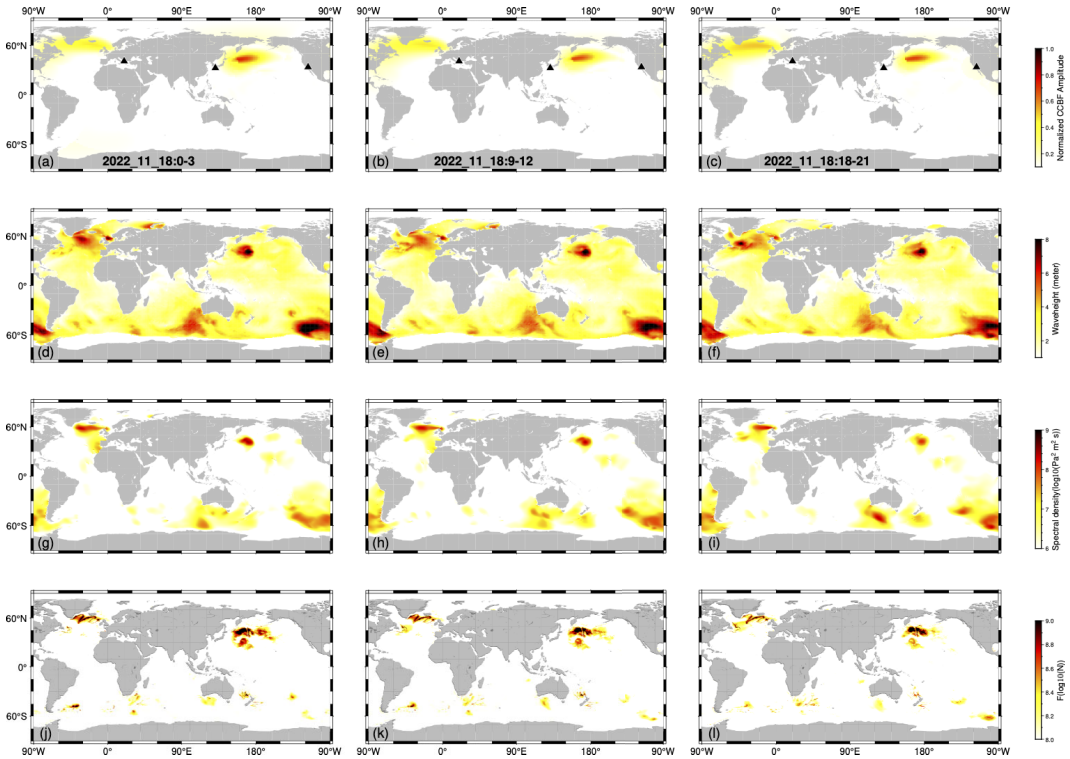

Figure A3. (a–c): Joint beam power map retrieved from the three networks based on 3-hr cross-correlation stacks and their back-projection on 2022 November 18 for three selected times (see labels). (d–f): Corresponding significant wave height maps from WW3 model. (g–i): corresponding averaged PSD of the ocean surface pressure field from 5 to 10 s extracted from the WW3 model. (j–l): the equivalent vertical force applied at the seafloor calculated with the WMSAN code.

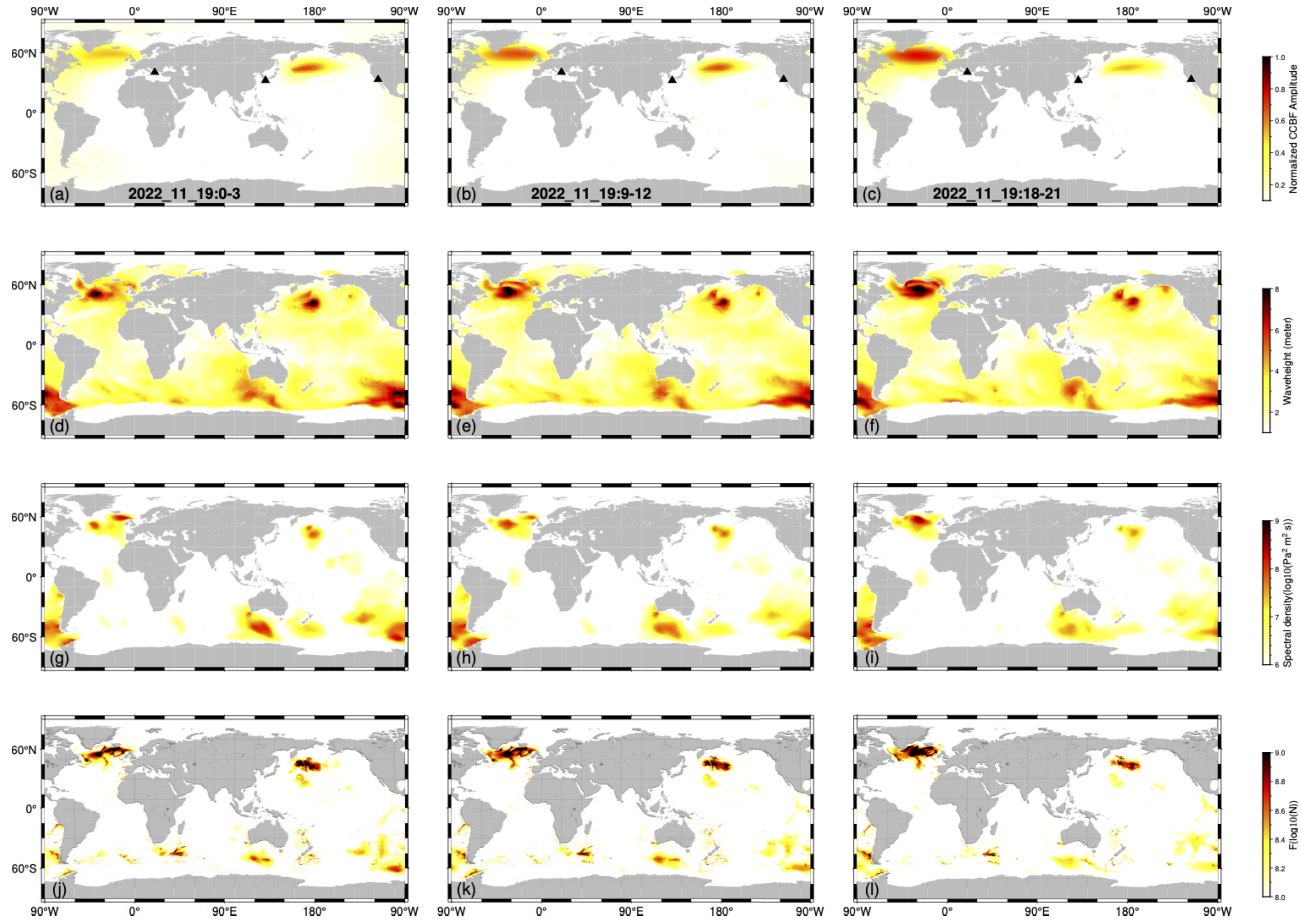

Figure A4. (a–c): Joint beam power map retrieved from the three networks based on 3-hr cross-correlation stacks and their back-projection on 2022 November 19 for three selected times (see labels). (d–f): Corresponding significant wave height maps from WW3 model. (g–i): corresponding averaged PSD of the ocean surface pressure field from 5 to 10 s extracted from the WW3 model. (j–l): the equivalent vertical force applied at the seafloor calculated with the WMSAN code.

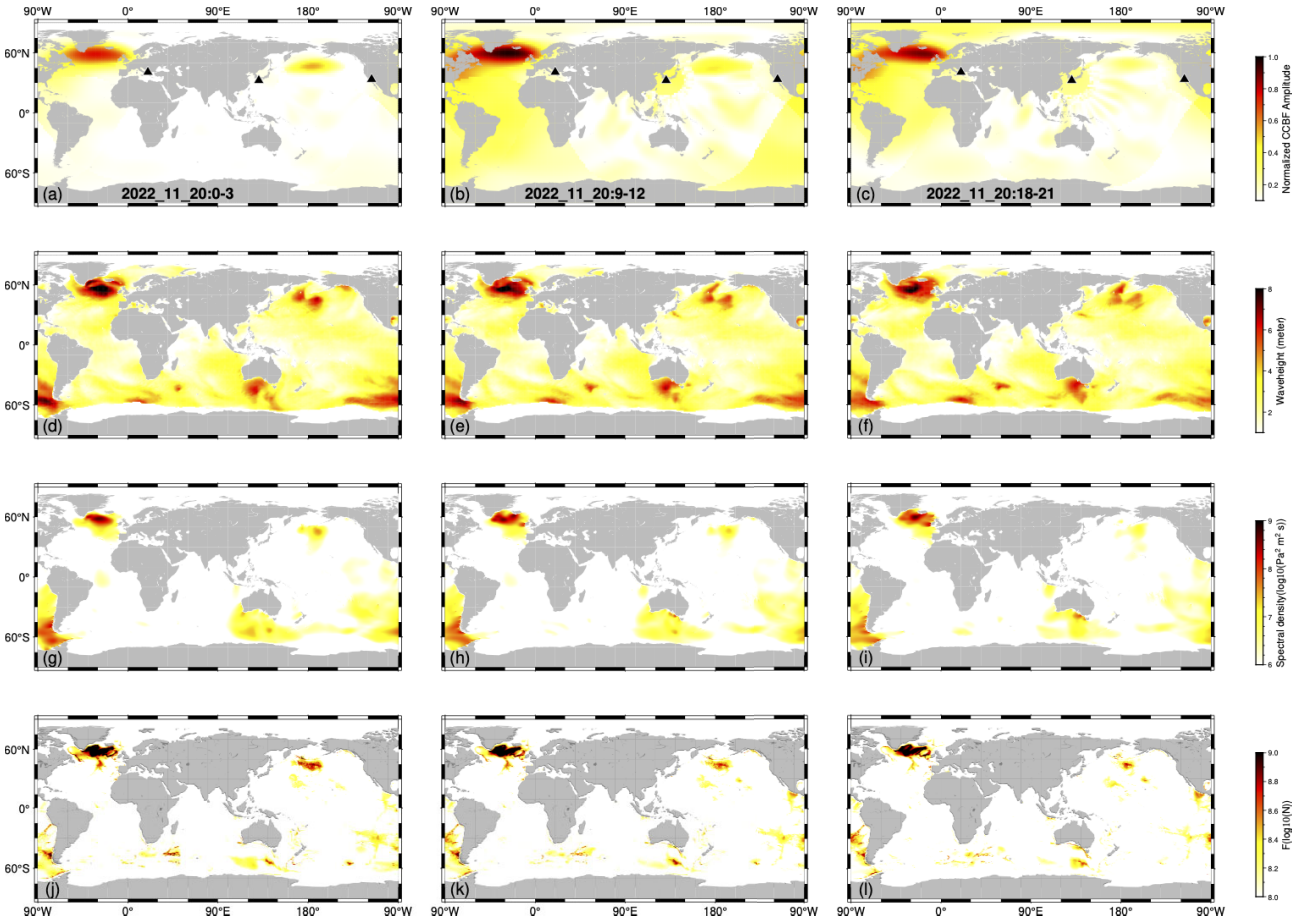

Figure A5. (a–c): Joint beam power map retrieved from the three networks based on 3-hr cross-correlation stacks and their back-projection on 2022 November 20 for three selected times (see labels). (d–f): Corresponding significant wave height maps from WW3 model. (g–i): corresponding averaged PSD of the ocean surface pressure field from 5 to 10 s extracted from the WW3 model. (j–l): the equivalent vertical force applied at the seafloor calculated with the WMSAN code.

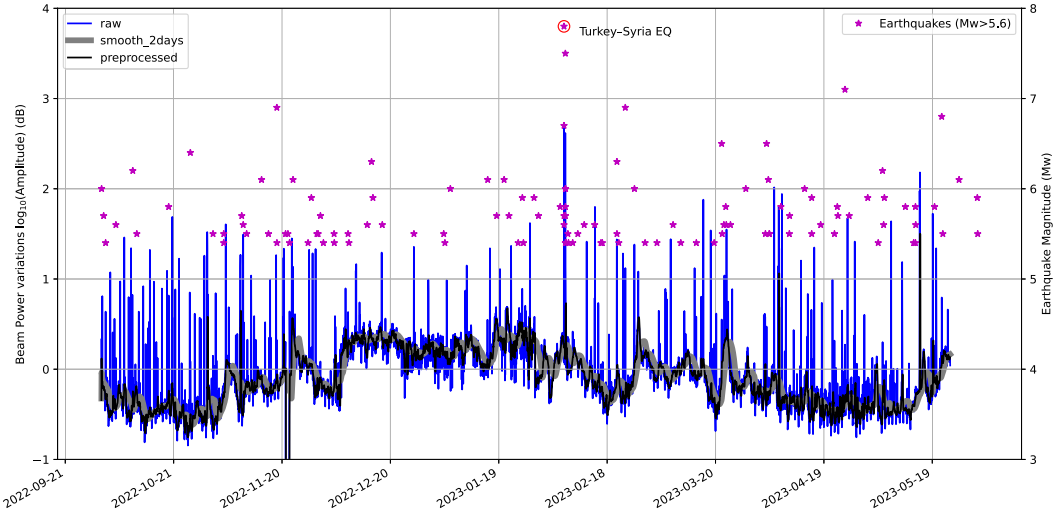

Figure A6. Comparison between the original beam power from RA beamforming and the pre-processed beam power. The fat grey line shows 2-d rolling mean and interpercentile range, 10th–90th percentile (IPR). The outliers, typically caused by strong local, regional (especially February 2023 Turkey-Syria events), and teleseismic earthquakes, are excluded by the pre-processing, as detailed in the text.

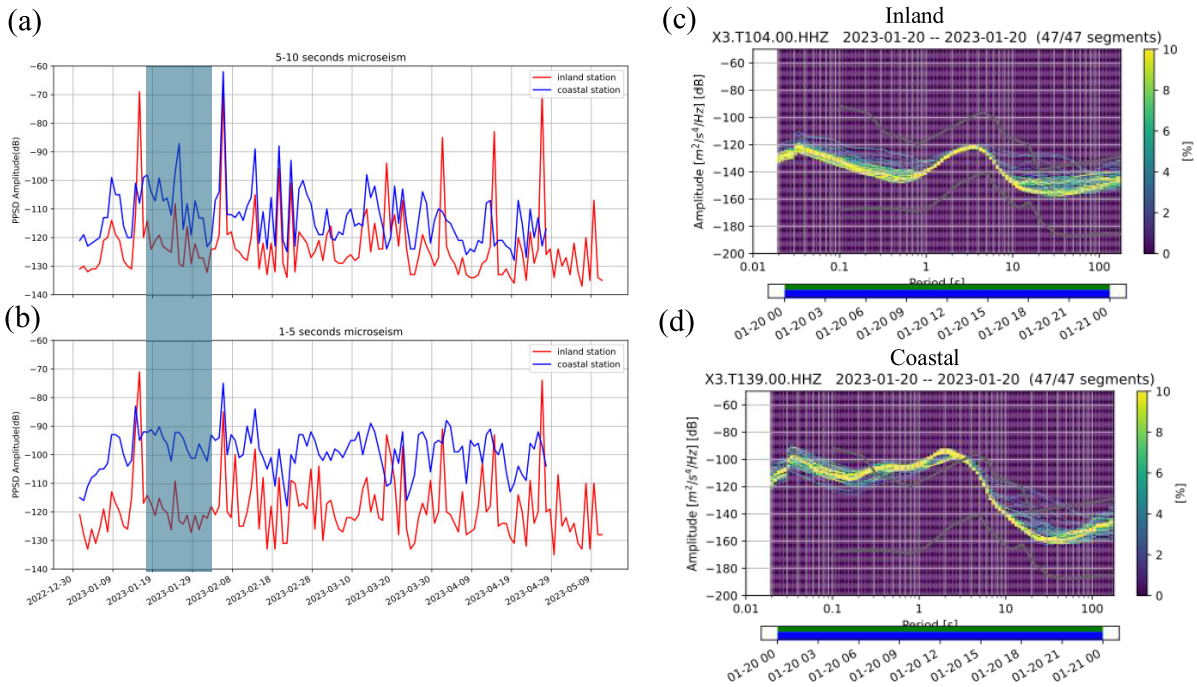

Figure A7. Comparison of noise characteristics at an inland ANTICS station (X3.T104) and a coastal ANTICS station (X3.T139). (a) Band-limited PSD amplitudes in the 5–10 s secondary microseism band (0.1–0.2 Hz) for December 2022–May 2023. The shaded area represents the date range of higher PPSD of costal station than inland station, which also display mismatch of the smoothed raw data beam power and equivalent force. (b) PPSD amplitudes in the 1–5 s band for the same period. (c–d) PPSD distributions for a representative day (2023 January 20) show consistently higher spectral levels at the coastal station in the 0.1–0.2 Hz band, by 10–20 dB, compared to the inland site.

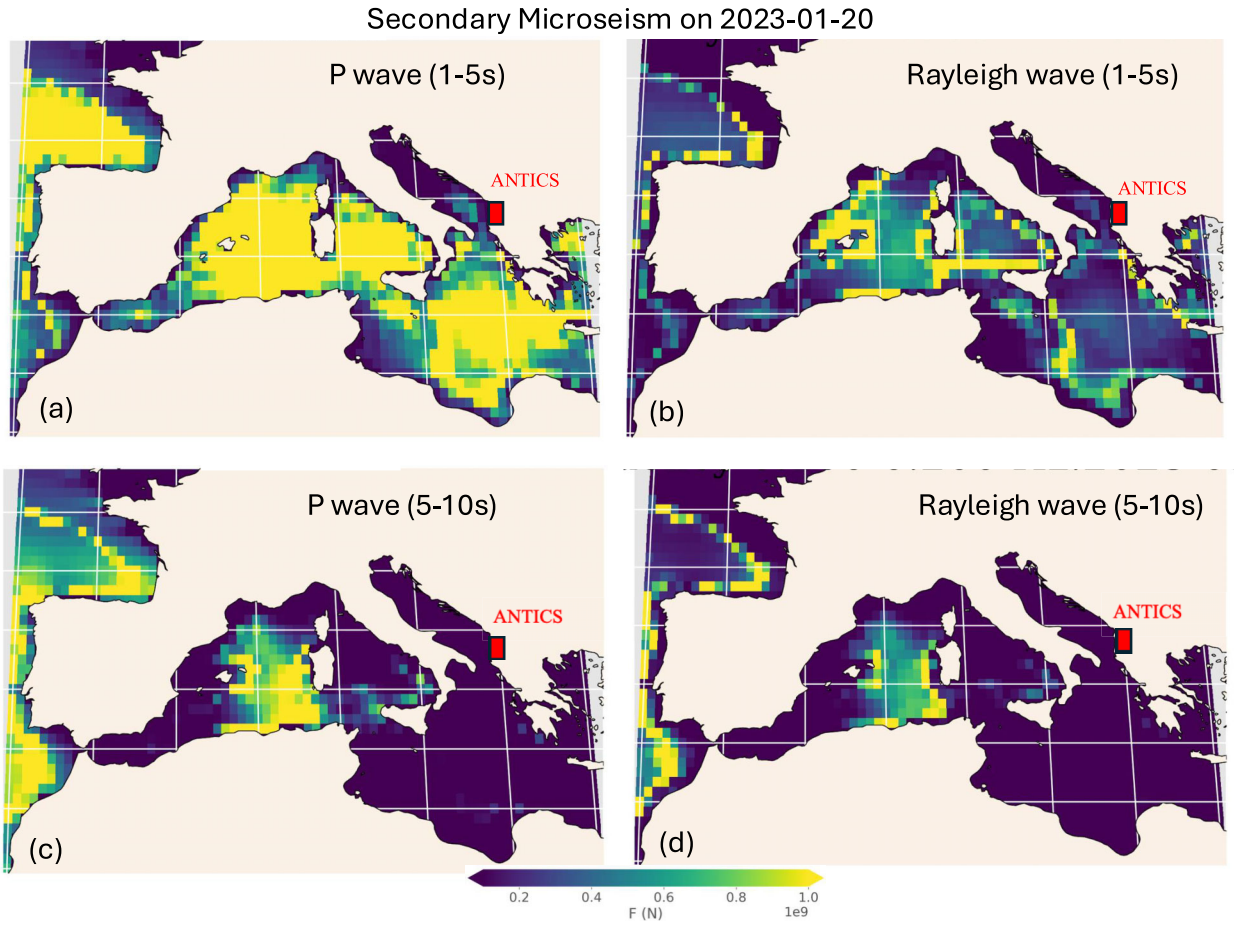

Figure A8. Computed *P* and Rayleigh wave secondary microseism sources (WMSAN) for the Mediterranean Sea on 2023 January 20. (a–b) 1–5 s (c–d) 5–10 s. The relatively weaker equivalent force of the microseism source of 5–10 s relative to 1–5 s also corresponds the elevated PPSD observed for the 1–5 s period from the inland station in Fig.A7

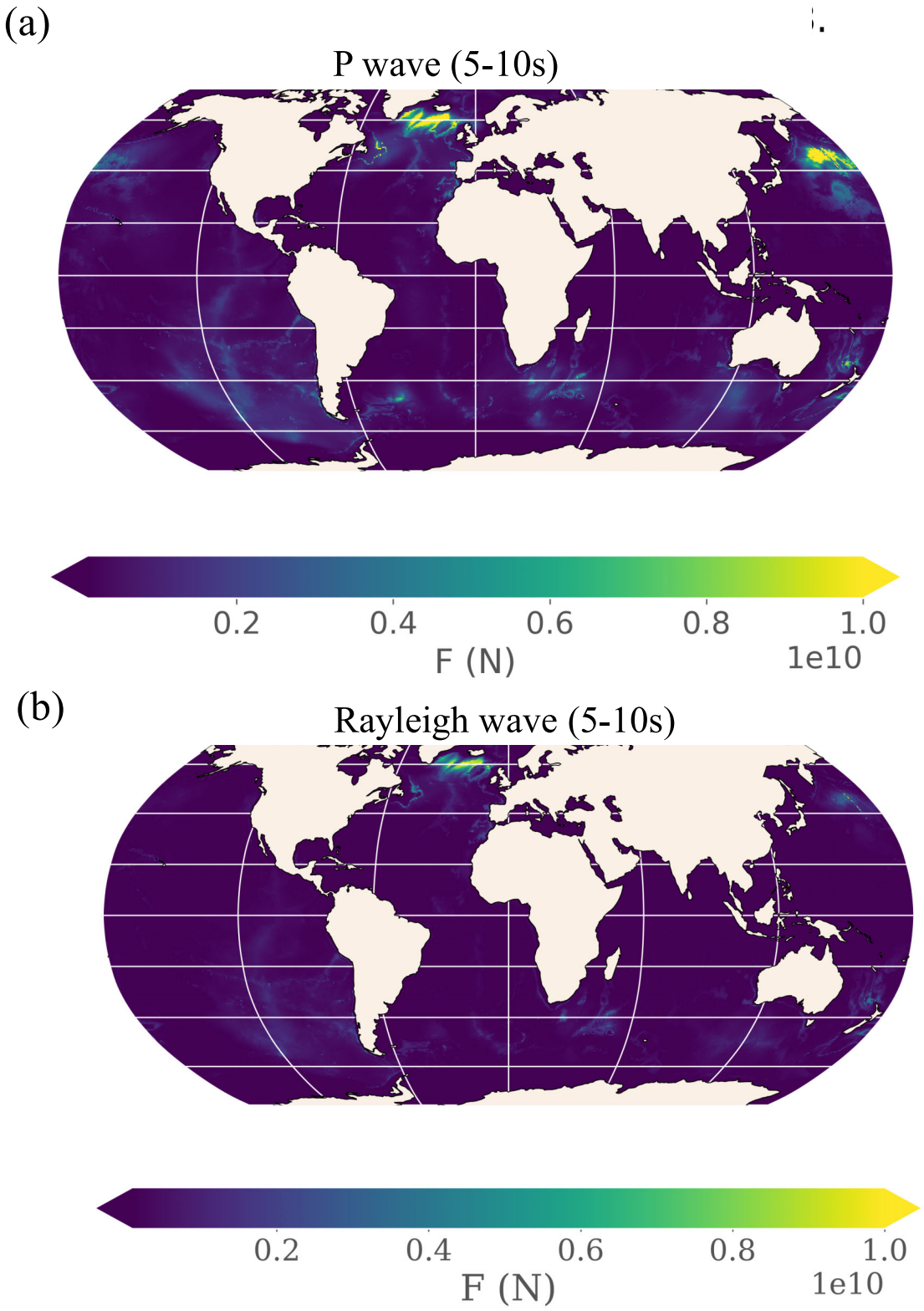

Figure A9. Computed global secondary microseism generation (WMSAN) on 2022 November 18. (a–b) 5–10s *P* wave microseism sources. (b) 5–10 s Rayleigh wave microseism sources.